International Journal of Multiphase Flow 35 (2009) 468–483

Contents lists available at ScienceDirect

International Journal of Multiphase Flow

journal homepage: www.elsevier.com/locate/ijmulflow

Experimental study on a non-dilute two-phase coflowing jet: Dynamics of particles in the near flow field

Luis M. Cerecedo *, Luis Aísa, Javier Ballester

Fluid Mechanics Department, LITEC-CSIC-University of Zaragoza, Maria de Luna, 3, 50018 Zaragoza, Spain

ARTICLE INFO

Article history:
Received 13 December 2007
Received in revised form 9 July 2008
Accepted 12 July 2008
Available online 27 July 2008

Keywords:
Particulate flows
Saffman lift force
Particle concentration

ABSTRACT

The dynamics of particles in multi-phase jets has been widely studied due to its importance for a broad range of practical applications. The present work describes an experimental investigation on an initially non-dilute two-phase jet, aimed at improving the understanding in this field. A two-color PDPA has been employed to measure simultaneously the velocity and size of particles. The measurements are post-processed to check the reliability of the results and to derive information on particle volume flux as an indication of their concentration. Acoustic forcing is applied in order to control coherent structures, which are responsible for mixing and transport phenomena, and also to get phase-locked measurements. Phase-averaged statistics enabled to *freeze* the jet structure, not visible in the time-averaged data. The results along the jet centerline confirm that drag forces and the spread angle of the jet initially control particle dispersion, very near the nozzle exit ($x/D < 4$). However, as the vortical structures evolve forming tongue-shaped structures, the total particle volume flux is augmented when these structures connect with the main stream ($x/D > 5$). This is due to an increase of the number of smaller size particles, even when a decrease of the number of larger size particle is observed. Further analysis at five cross-stream sections across two consecutive vortices confirm that small particles are convected around the coherent structure and then incorporated to the main stream, increasing the particle concentration at the jet core. On the other hand, the number of larger particles (as well as their contribution to axial volume flux) starts to decay in regions of high azymuthal vorticity. This behaviour is partly ascribed to the transversal lift force, associated to the large spatial gradients observed in these regions. Saffman and Magnus forces have been estimated to be comparable or even greater than radial drag forces. The results suggest that the Saffman force might accelerate particles in radial direction, inducing a high radial volumetric flow rate from high to low axial velocity regions.

1. Introduction

The knowledge on particle concentration in multi-phase jets is an important topic, due to its relevance for many industrial applications. For instance, particle dispersion and concentration greatly influence the performance and efficiency of combustion systems. In spite of significant advances in computational methods, many experimental investigations have been conducted on these flows in order to improve their understanding and explain some peculiar behaviors.

Maxey and Riley (1983) developed the general expression for the fluid forces acting on a small rigid sphere. After the latter work, many researchers scrutinized how particles behave in cases with small ratios of gas and particle densities, frequently in dilute regimes (i.e., low loading mass ratio). Maxey and Riley expressed the particle acceleration in terms of the aerodynamic drag force, the pressure gradient, the virtual mass induced drag, the weight and the Basset history force. An order of magnitude analysis (Chung and Troutt (1988), Sbrizzai et al. (2004)) has revealed that the forces caused by the virtual mass and the pressure gradient are of the order of the density ratio (ρ_g/ρ_p), and the Basset force is of the order of $(\rho_g/\rho_p)^{1/2}$, while the drag (the *dominant force*) is of the order of characteristic time ratio (t_g/t_p). In the present investigation, $\rho_g/\rho_p < 5{*}10^{-4}$, and, thus, the drag and gravity forces are considered as the relevant terms in the particle motion equation, which takes the form

$$\frac{d\mathbf{u}_p}{dt} = -\frac{3}{4}\frac{C_D}{d_p}\frac{\rho_g}{\rho_p}|\mathbf{u}_g - \mathbf{u}_p|(\mathbf{u}_g - \mathbf{u}_p) + g \tag{1}$$

$\mathbf{u}(u,v,w)$ is the velocity, C_D the particle aerodynamic drag coefficient, ρ is the density, d_p is the particle diameter, and $\mathbf{g}$ is the gravity acceleration. Subscripts g and p denote gas and particle variables, respectively. Should l_c and U_c be suitable characteristic length and velocity scales, Eq. (1) can be rewritten in dimensionless form as

$$\frac{d\mathbf{u}_p^*}{dt^*} = \frac{1}{S_t}(\mathbf{u}_g^* - \mathbf{u}_p^*) + \frac{1}{F_r} = F_D + F_g \tag{2}$$

S_t is the Stokes number, F_r the Froude number, and F_D and F_g stand for dimensionless drag and gravity forces, respectively. The star is used for dimensionless variables.

* Corresponding author. Fax: +34 976 76 18 82.
E-mail address: cerecedo@litec.csic.es (L.M. Cerecedo).

0301-9322/$ - see front matter © 2008 Elsevier Ltd. All rights reserved.
doi:10.1016/j.ijmultiphaseflow.2008.07.003

Based on Maxey and Riley investigation, Chung and Troutt (1988) proposed that particle dynamics in the near flow field of a jet is controlled by large-scale structures. Martin and Meiburg (1994) emphasized that idea. This motivated the use of acoustic forcing in a number of works to control and enhance coherent structures in order to gain further insight into particle dispersion phenomena. Among others, Longmire and Eaton (1992), Lázaro and Lasheras (1992a,b), and Swanson and Richards (1997), demonstrated that particle concentration depends not only on particle size but also on the flow field induced by large-scale structures. For example, Longmire and Eaton (1992), using Particle Image Velocimetry, PIV, and Aísa et al. (2002), using Phase Doppler Particle Analyser, PDPA, showed that particles with Stokes numbers, St, up to ~6, disperse more effectively in the flow field. This is consistent with the value of St obtained by Martin and Meiburg (1994) in a computational simulation. Moreover, Longmire and Eaton (1992) found that the limit of St for particle dispersion increases up to 12 when external forcing is applied. Differences between both results tend to confirm that large-scale structures play an important role on the distribution of particles within the flow field. However, the question pertaining to how the motion of particles in the near field is affected by these structures still remains.

On the other hand, Lázaro and Lasheras (1992b) and Longmire and Eaton (1992), among others, demonstrated that particles altered the basic flow structure even for a dilute regime, and that streamwise gas-particle slip velocity increased at the jet exit as the particle mass loading ratio (defined as the ratio of particle to air mass flow rates) became larger (Park and Chen (1989)). Swanson and Richards (1997) also showed that the slip velocity was higher when the gas-phase axial mean velocity increased at the jet nozzle. It should be noticed that, as the slip velocity significantly departs from zero, the hypothesis that the Reynolds number, based on the relative gas/particle velocity, is much smaller than unity, essential to used Stokes' drag, is no longer fulfilled.

Although some investigators ascribed particle dispersion only to aerodynamic drag (Longmire and Eaton (1992), Martin and Meiburg (1994), and Anderson and Longmire (1995)), others like Bagchi and Balachandar (2002a,b), Cherukat et al. (1999), Kurose and Komori (1999), and You et al. (2003) observed that for locally sheared flows the vortex structure might cause particle dispersion through Saffman forces and Magnus effects. The latter were suggested to significantly contribute to the radial particle dispersion.

In a previous work, Cerecedo et al. (2004) analyzed the changes of flow structure caused by forcing; their results indicated very large spatial gradients of the axial velocities induced by the generated large-scale structures. This suggested that both Saffman and Magnus effects should be taken into account in the general particle motion equation, specially for flows with spatial velocity gradients, **G** (See Fig. 1).

If the particle is convected along by a vortical structure and the flow is directed downward, the axial and radial equations of particle motion for u_p and v_p, respectively, are given by

$$\begin{aligned} m_p \frac{du_p}{dt} &= -\frac{3}{4}\frac{C_D}{d_p}\frac{\rho_g}{\rho_p} m_p |u_g - u_p|(u_g - u_p) + m_p g \\ m_p \frac{dv_p}{dt} &= -\frac{3}{4}\frac{C_D}{d_p}\frac{\rho_g}{\rho_p} m_p |v_g - v_p|(v_g - v_p) + m_p \omega^2 r - F_{ls} - F_{lr} \end{aligned} \tag{3}$$

where m_p is the particle mass, $\boldsymbol{\omega}$ is the vorticity, and F_{ls} and F_{lr} are the lift forces due to shear and to particle rotation, respectively.

The present work is aimed at describing gas/particle interactions in the near flow field (where large-scale structures are visible) of an initially non-dilute two-phase jet. Acoustic forcing is applied to enhance large-scale structures, and to get phase-averaged (phase-locked) measurements. The initial loading mass ratio is 0.3, corresponding approximately to 40% of that of a stoichiometric mixture of a liquid hydrocarbon fuel. For the flow velocity, particle characteristics and loading mass ratio used in this work, a large axial slip velocity between phases is obtained at the nozzle exit, where conditions for Stokes' drag are therefore not fulfilled. In order to *freeze* coherent structures phase-averaged statistics, defined as the ensemble average of many realizations occurring at a specific time phase in the forcing cycle, are obtained with a two-color Phase Doppler Particle Analyzer (PDPA). Taking advantage of the phase-locked measurements, particle concentrations along the jet centerline and at five different downstream cross sections corresponding to the spatial evolution of a vortical structure are analysed in terms of the axial particle volume flux (ψ_x) and radial volumetric flow rate (g_r). Some comparisons are made with the results obtained by Aísa et al. (2002), who measured time-averaged variables for the same unforced jet. Conclusions are drawn on how coherent structures can influence particle dispersion.

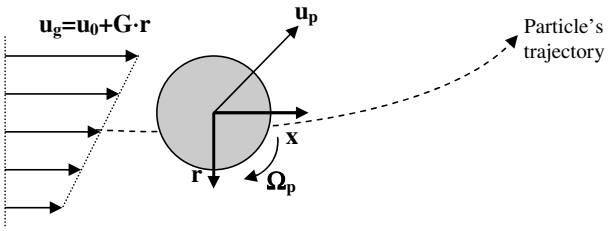

Fig. 1. Particle traveling in a shear flow. High spatial gradients or particle rotation alter particle trajectory by Saffman and Magnus effects, respectively.

2. Experimental facilities

2.1. Jet rig

The experimental setup has been described in previous works (Aísa et al. (2002), Cerecedo et al. (2004)), and only a brief reminder is provided here. The facility (Fig. 2) consists of an air supply system, a nozzle with a contraction coefficient of 5.13, a methacrylate chamber, and particle feeders (cyclone-like for tracers and vibrating device for solid-particles). A compressor provides the main air flow, the flow rate being measured with an orifice plate. The air flows vertically downward through a pipe 77D long and discharges through a nozzle ($D = 12$ mm) mounted inside the methacrylate chamber. The latter has a square cross section of 480×480 mm^2 and is 1.15 m long. The mean discharge air velocity at the nozzle exit (U_0) is fixed at 15 m/s for all the studied jets, with a resulting Reynolds number of 1.2×10^4 based on the nozzle diameter. A low velocity (0.2 m/s) secondary air stream (coflow) is induced inside the chamber by a fan.

A loudspeaker, installed on the opposite side to the nozzle in order to acoustically force the jet, is fed with a sine wave signal, generated by a filtered train of pulses from a Transistor–Transistor-Logic Circuit (TTL). To acquire phase-averaged measurements, burst detection is inhibited at all times except during a 15° window, initialized on the 0° phase of the forcing signal. The same TTL circuit is employed to inhibit the data acquisition, avoiding time delays.

Cerecedo et al. (2004) pointed out that there exists a simple statistical relationship between *time-averages*, $\bar{\eta}(t)$, and *phase-averages*, $\langle\eta(\phi)\rangle$,[1] through the equation

$$\overline{\eta(t)} = \frac{1}{2\pi}\int_0^{2\pi} \langle\eta(\phi)\rangle \mathrm{d}\phi \tag{4}$$

Cerecedo et al. (2004) identified 400 Hz as the principal frequency for the generated flow. Thus, the jet is acoustically forced at this fre-

[1] In the present work, phase-averaged (also called phase-locked) properties are denoted by brakes "⟨⟩". For time-averages the overbar will be omitted.

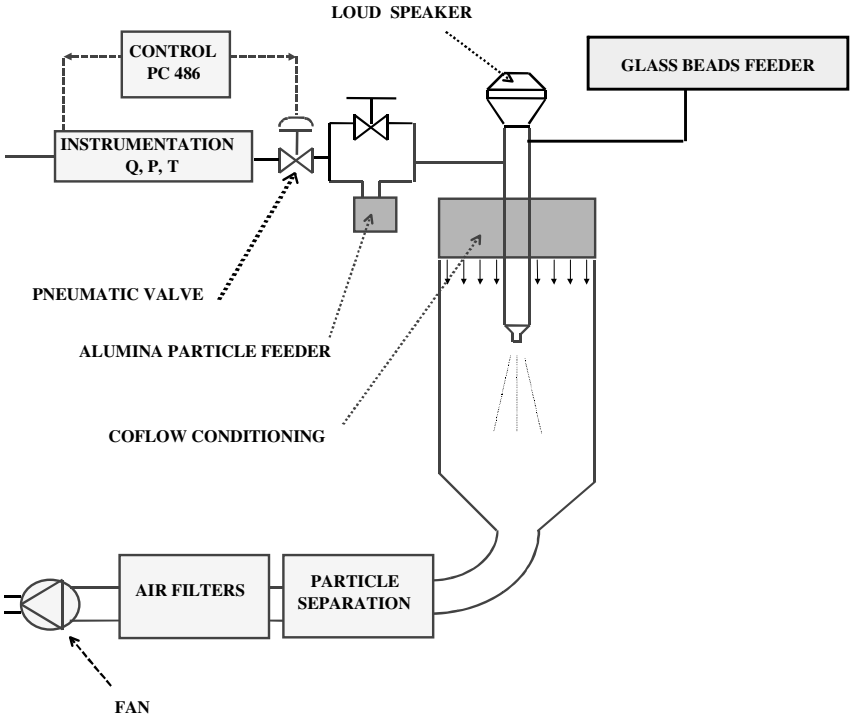

Fig. 2. Experimental setup.

quency with a signal amplitude of 8 V_{pp}. The results from Aísa et al. (2002) on the unforced jet are used for comparison.

2.2. Measurement system

Velocity and particle size measurements are performed with a dual-beam TSI-Aerometrics PDPA interferometer, with a FFT signal processor Mod. 3100. Forward scattering with detection at 30° from the transmitter optical axis is used. The tracer for the gas-phase is alumina powder ($d_A < 0.3$ microns) and the solid-phase consists of spherical glass beads with a measured density of 2340 (kg/m^3); the condition $\frac{\rho_g}{\rho_p} \ll 1$ is fulfilled. The initial loading mass ratio $\left(\frac{m_{solid-phase}}{m_{gas-phase}}\right)$ is 0.3. This value is used for all tests reported here, and is checked every 10 min, displaying time variations not greater than 7%.

Measurements of the solid-phase (velocity, size and transit time of glass spheres) are made in the absence of alumina tracers. Only for the measurements of gas velocities, the two-phase flow is simultaneously seeded with both the tracers and the glass beads. The particle discrimination method is applied in order to differentiate between tracer and solid-particles; comparisons between the results of both data files indicates a maximum deviation of 7% in the mean axial velocities, of 1.8% in the rms of fluctuations and of 3.4% in Reynolds stress values.

All data reported in the present work are post-processed in order to diminish the velocity bias. The particle transit time is used as the weight factor, c_i, according to

$$U_{cor} = \frac{\sum c_i \cdot U_i}{\sum c_i} \tag{5}$$

2.3. Particle conditioning

As a first step, particles were sieved to a nominal size band of $30 < d_p < 110$ μm. A sample of 2958 particles was observed through an optical microscope, with a resolution of 5 μm. These results were compared with those obtained with the PDPA at the jet centerline, at 0.5D from the nozzle exit. Fig. 3 shows the diameter histogram as obtained with the microscope. A good agreement is apparent in the mean diameter value for both microscope and PDPA measurements (errors <0.1%); however, rms values display significant deviations (≈35%). This discrepancy is ascribed to uncertainties in the measurement techniques (bias in the PDPA technique, microscope resolution, appreciation errors, etc.), and to the fact that some particles were not perfectly spherical (≈5%). Another important source of bias can be the particle focalization at the jet exit, as it will be shown below. This high particle density observed at the jet centerline causes some particle rejection that biases the arithmetic averages. Nevertheless, these results are thought to provide an indication of the good quality of the measurements.

In order to avoid statistical deviations due to low particle counts results are grouped into 5 size classes, with the limits shown in Table 1. The particle aerodynamic response time, $t_p = \frac{\rho_p d_p^2}{18\mu}$, assum-

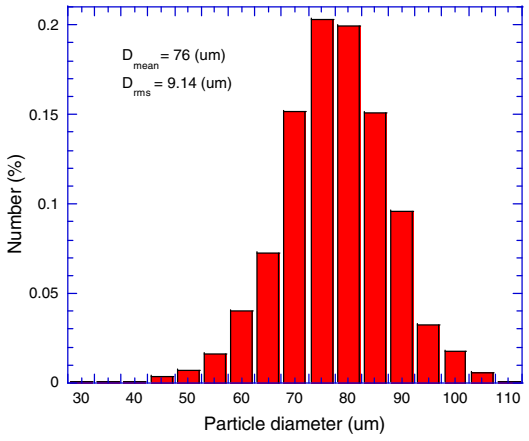

Fig. 3. Diameter histogram of glass beads (solid-particles). Microscopy counting.

Table 1
Particle size classes used in the present work

Particle size classes (μm)	Mean diameter $(d_{max}–d_{min})/2$ (μm)	Particle number	Percentage number (%)	Equivalent t_p in the Stokes regime (ms)
30–65	47.5	466	15.75	6.5–30.5
65–75	70	1156	39.0	30.5–40.6
75–85	80	1047	35.40	40.6–52.2
85–110	97.5	289	9.78	52.2–87.4

For comparison with other investigations, the particle aerodynamic response time, should Stokes regime be considered, is also shown.

ing Stokes regime is also shown for comparison with other authors, although conditions for its existence are not fulfilled in the present work.

2.4. Particle volume flux measurements

One important parameter associated with the particle concentration (Widmann et al. (2001) and Aísa et al. (2002), among others) is the particle volume flux (ψ). It is obtained from the volumetric flow rate as

$$\psi_i = \frac{1}{T}\sum_i \frac{\pi}{6}\frac{d_{pi}^3}{A_i} \ (\mathrm{cm}^3/\mathrm{cm}^2\ \mathrm{s}) \tag{6}$$

where d_{pi} is the particle diameter of the i^{th} class that crosses the effective probe area A_i, and T is the total time period for the measurement.

Post-processing based on the Generalised Integral Method (GIM), proposed by Aísa et al. (2002), is applied in order to obtain the corrected axial volume flux (ψ_{xi}). In addition, the statistical correction method for the count error due to multiple particles in the probe volume, introduced by Roisman and Tropea (2000), is also used; this compensates those signals rejected due to the high particle density observed near the jet centerline, which underestimate the actual particle number convected through the measurement volume.

2.5. Radial volumetric flow rate calculations

A complete description of the particle distribution is achieved by calculating the radial volumetric flow rate (g_{ri} [mm^3/s]), through a mass balance on the particles. Control volumes are concentric annular boxes bounded by two cross sections (Fig. 4).

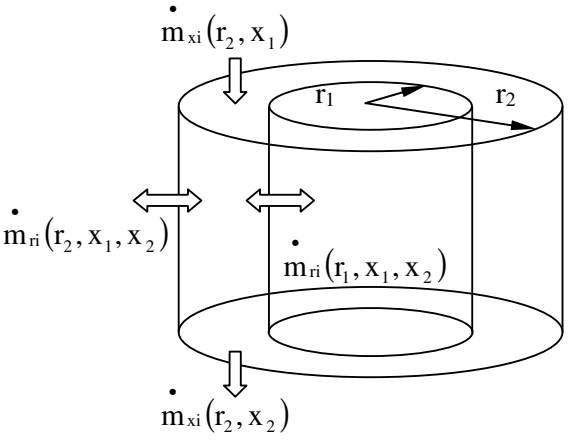

Fig. 4. Control volume used for calculation of radial flow rates.

Since the particle density is constant and neither particle breaking nor particle coalescence occur in the present flow, the mass flux balance can be written as

$$\dot{m}_{ri}(r_2, x_1, x_2) = \dot{m}_{ri}(r_1, x_1, x_2) + \dot{m}_{xi}(r_2, x_1) - \dot{m}_{xi}(r_2, x_2) \tag{7}$$

or, in terms of volumetric flow rates,

$$g_{ri}(r_2, x_1, x_2) = g_{ri}(r_1, x_1, x_2) + g_{xi}(r_2, x_1) - g_{xi}(r_2, x_2)\ [\mathrm{mm}^3/\mathrm{s}] \tag{8}$$

with

$$g_{xi}(r_2, x_j) = \int_{r_1}^{r_2} \psi_{xi}(r, x_j) 2\pi r\, dr \tag{9}$$

$\dot{m}_{ri}(r_1, x_1, x_2)$ is the radial mass flux through the inner cylindrical surface, $\dot{m}_{xi}(r_2, x_1)$ stands for the axial mass flux that enters Section 1 and $\dot{m}_{xi}(r_2, x_2)$ for the axial mass flux that exits Section 2. g_r and g_x are the volumetric flow rates in the radial and axial directions, respectively.

3. Results

3.1. Jet injection conditions

The time-averaged axial velocity ($\overline{u(t)} = U$) profiles of both the gas and the solid phases at the nozzle exit are shown in Fig. 5a. Velocities are normalized with the gas-phase velocity at the jet centerline. Due to beam access limitations, the first measured section is located 0.5D downstream from the nozzle. For comparison, the unforced case (Aísa et al. (2002)) is also plotted. These results confirm the good symmetry of the jet, and reveal the existence of high axial slip velocities at the injection. This is consistent with the idea that particle velocities are considerably lower than those of the gas-phase because particles cannot follow the rapid fluid acceleration in the nozzle. Particle velocities ranged from about 48% to 54% of those of the gas. Swanson and Richards (1997) have observed that the axial slip velocity increases with the Reynolds number based on gas velocity and diameter nozzle. Sakakibara et al. (1996) have also reported axial slip velocities at the exit of a lightly loaded forced jet, with particle velocities 55% of those of the fluid.

Profiles of the phase-averaged axial velocity for both gas and solid phases at the nozzle (not shown here) are similar to those depicted in Fig. 5a. This behavior is consistent with the results of Cerecedo et al. (2004) showing that the coherent fluctuation does not influence the arithmetic mean when time-averages are considered.

The profile of particle axial volume flux is shown in Fig. 5b. The occurrence of particle focalization is apparent, and is also corroborated by flow visualization (Fig. 12 below). Hayashi and Branch (1980) also observed a high particle density at the jet centerline in a pioneer experimental study on a gas/solid two-phase jet with ash particles (solid-phase mean diameter 24 microns). This result reveals that jet forcing does not modify the distribution of particles over the nozzle cross section, as Anderson and Longmire (1995) have also observed for a similar jet.

Integration of the particle axial volume flux profile (Fig. 5b) underestimates by 11% the mass particle rate actually injected. This deviation is comparable to the uncertainty in the initial loading mass ratio (7%), and can also be taken as a measure of the uncertainty of the results reported in this work. In addition, remarkable similarities between the unforced (Aísa et al. (2002)) and forced jets (present work) should be pointed out.

On the other hand, as expected, time- and phase-averaged results of the axial volume flux can lead to different results, as the second includes only a fraction of the particles crossing the measuring volume. This is confirmed by Fig. 6a, where particle volume

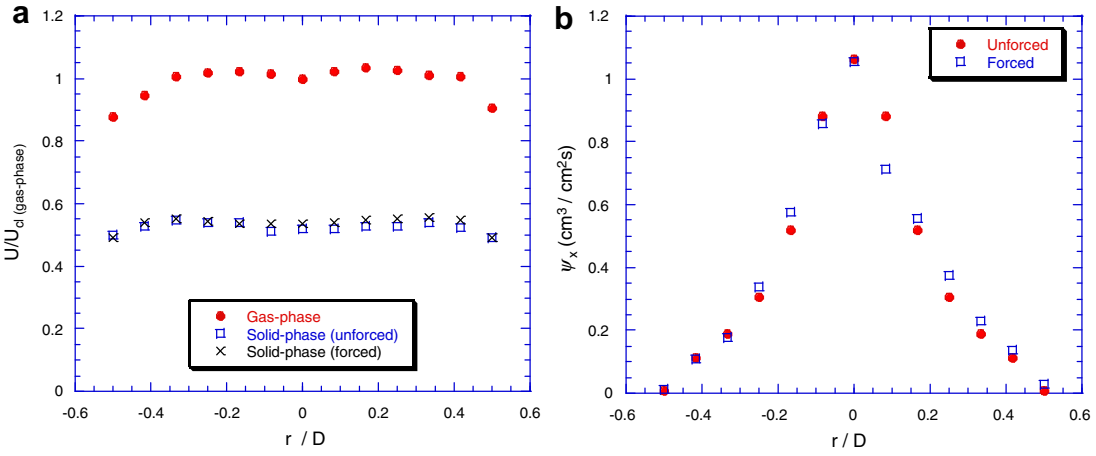

Fig. 5. Profiles of time-averaged axial velocities and axial volume flux at the nozzle exit ($x/D = 0.5$). Comparison to the unforced case (Aísa et al. (2002)). (a) Axial velocity profiles. (b) Axial particle volume flux.

flux is shown for the forced jet in terms of both time-averages (ψ_x) and phase-averages ($\langle\psi_x\rangle$), normalized with the time-averaged value at the jet centerline (ψ_{xcl}). However, this difference vanishes when both are normalized with their own maximum value at the jet centerline (see Fig. 6b).

The contribution of every particle size class (d_{pi}) to the phase-averaged volume flux is shown in Fig. 7a, where the results are normalized by the total volume flux at the jet centerline found in the window $0° < \phi < 15°$. Since the volume flux is a function of the particle diameter cubed (see Eq. (6)), Fig. 7b might be a better way to present the results, with particle volume flux for each size classes normalized by their own value at the jet centerline. Radial profiles of the axial volume flux calculated in this manner are similar, indicating a homogeneous particle distribution, as also found by Hayashi and Branch (1980). Therefore, the probability to find any particle size class at a fixed-point seems to scale with the maximum value encountered at the jet centerline.

Fig. 8 displays the phase-averaged rms fluctuations for both axial (u^0) and radial (v^0) components. The single-phase flow is plotted for comparison. As expected, very low rms values of both gas and single phases are measured, due to the nozzle geometry limiting the turbulence levels. Differences are noticeable only in the outer zone of the jet.

The standard deviation of the particle (solid-phase) axial velocity is more uniform over this section, and significantly higher than that for the gas. This behavior might be ascribed to the averaging over all particle sizes, each one having a different mean velocity (see Fig. 9), and is consistent with the results of Sakakibara et al. (1996).

Although rms values are statistical parameters defined mathematically in the same way for all particles (tracers and glass beads), their meaning is somewhat different for the two phases. For gas-phase measurements, the tracer (small particles) is considered to move at approximately the gas-phase velocity and, thus, is indicative of the *velocity fluctuations* as they are convected past the measurement volume. On the other hand, rms values for the solid phase are named as *standard deviations* in order to see the discrete-phase from a Lagrangian viewpoint.

A more precise description is obtained when the results are classified into different particle size ranges (as defined in Table 1). The radial profiles of phase-averaged axial velocities are shown in Fig. 9. The values are normalized with the velocity averaged over all the size classes at the jet centerline (*cl. all sizes*). These results emphasize the relationship between the particle size and the axial slip velocity; the larger the size, the higher the axial slip velocity. This is consistent with previous observations, reported by Prévost (1994), Swanson and Richards (1997) and García (2000), on

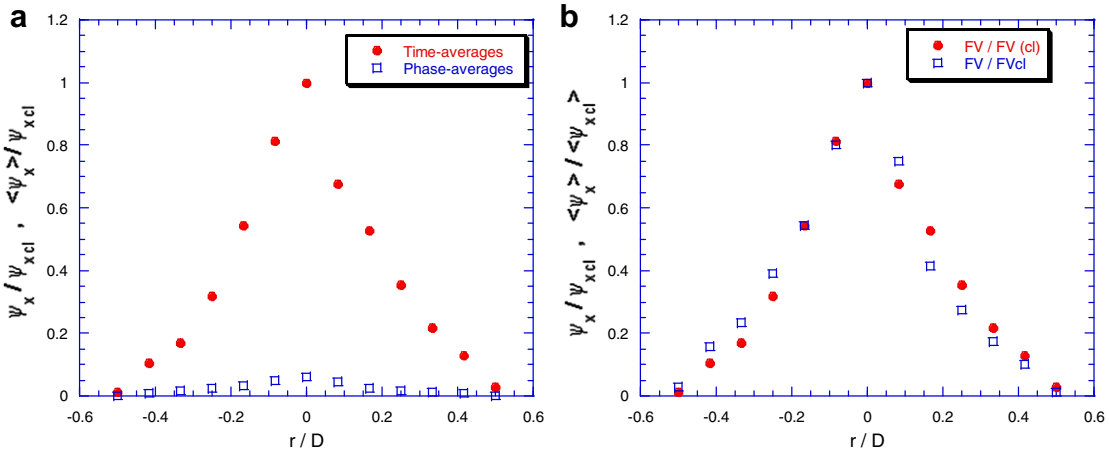

Fig. 6. Time and phase-averaged particle volume flux at the nozzle exit. (a) Both are divided by the maximum time-averaged value found at the jet centerline (b) Each of them is divided by its own maximum value at the jet centerline.

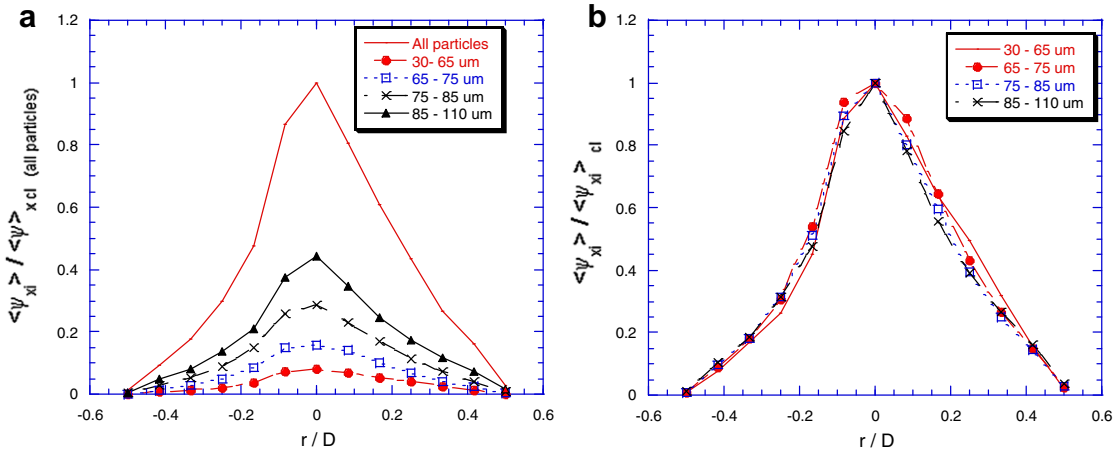

Fig. 7. Contribution of each particle size class to the total particle volume flux at the nozzle exit ($x = 0.5D$). Phase-averages.

unforced jets. As mentioned before, differences between velocity values for the various size classes are responsible for the high standard deviations observed in Fig. 8.

3.2. Evolution along the jet centerline

The evolution of the axial particle volume flux for each size class along the jet centerline is shown in Fig. 10a. Using the results of Fig. 7b, the particle volume fluxes are made dimensionless with the maximum value at the nozzle exit for each particle size class ($\langle\psi_{xi}\rangle_{0cl}$). A *smoothing* curve, generated by adjusting the experimental data with a locally weighted Least Squares Method, is plotted for comparison. As suggested by Cerecedo et al. (2004), such a curve can be seen as the first approximation to the *time-averaged behavior expected* in the axial volume flux, if all phases ($0 \leqslant \phi \leqslant 360°$) were averaged. Mathematically

$$\frac{1}{2\pi}\int_0^{2\pi}\langle\psi(\phi)\rangle \mathrm{d}\phi = \overline{\psi(t)} = \psi_x \tag{10}$$

It is interesting to notice that the evolution of the phase-averaged axial volume flux in Fig. 10a shows an oscillating, decaying trend for all size classes, although the profiles are not similar. In fact, a spatial delay between two peaks exists among the different particle sizes (Fig. 10b and c). These oscillating patterns are similar to those found for the evolution of gas and particle velocities along the jet centerline (Fig. 11), and have a common origin. Since the phase-averages are well correlated with the large-scale structures, the amplitude and spatial locations of the peaks of axial volume fluxes confirm that the particle concentration depends on the flow pattern as well as on the particle size.

Although gas and particle velocities indicate that the effect of large-scale structures is no longer appreciable beyond $x/D \approx 9$ (Fig. 11), oscillations in particle axial volume flux survive for longer distances and only tend to vanish at the end of the studied zone. This can be interpreted as clusters (groups of particles) traveling together. This might explain the results of Hayashi and Branch (1980), who reported concentrations that were independent of particle size.

The evolution of phase-averaged axial volume flux along the jet centerline (Fig. 10) also reveals another interesting effects. Distinct behaviors can be identified as a function of the particle size:

- The results obtained for finer particles (Fig. 10a and b) display some particular features: (i) near the nozzle exit ($x/D < 4$) their concentration decreases more rapidly along the jet centerline than larger sizes, but displays higher values at the second peak observed ($4 < x/D < 6$). This suggests that, at the very near flow field, smaller particles are convected around the vortical structure and, then, some of them are reincorporated into the main stream (the jet centerline); (ii) a directional classification due

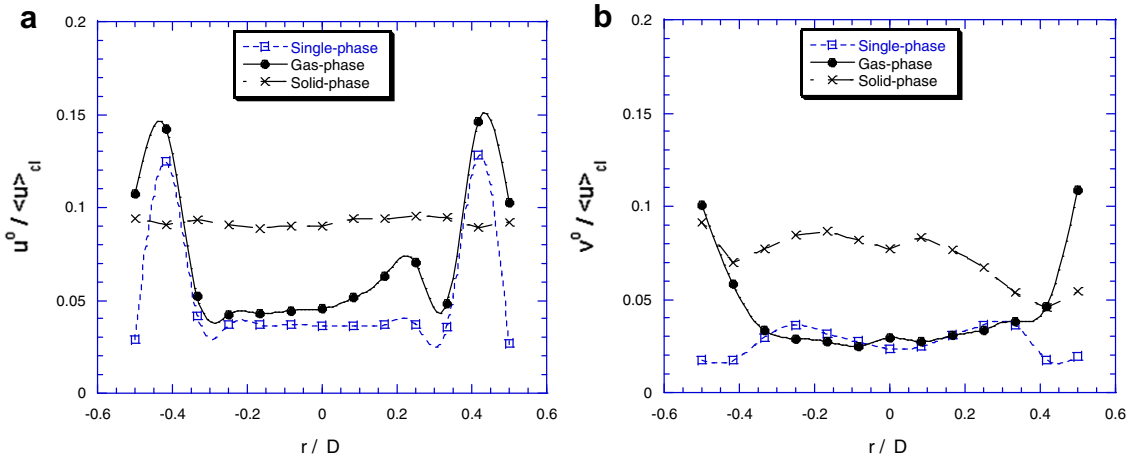

Fig. 8. Radial profiles of the rms fluctuations at the nozzle exit ($x = 0.5D$). (a) Axial velocity. (b) Radial velocity.

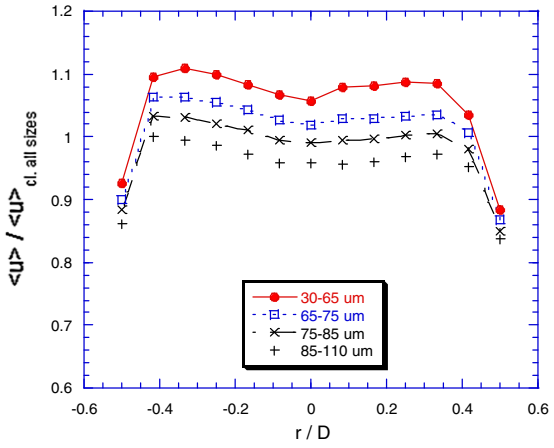

Fig. 9. Phase-averaged velocity profiles of the solid-phase for the different particle size classes. Axial velocities are normalized with the average of all of them at the jet centerline (*cl. all sizes*).

to the jet spread angle is thought to contribute to particle concentration very near the nozzle; and (iii) when $x/D > 5$, the amplitude of oscillations (associated to the concentration) decays faster than for larger sizes, likely because they are again trapped in the vortex, are centrifuged outwards from the structure and forced away from the jet.

- The remaining classes (Fig. 10c) depict similar qualitative evolutions among them. However, it is interesting to note that as the particle diameter increases: (i) oscillations show a delay in their own amplifications (the highest peak moves downstream), attributed to inertial effects (larger particles are more difficult to accelerate); and (ii) subsequent peaks undergo an advance in the spatial phase (peaks move towards the nozzle exit as the size increases). This is consistent with observations made by Sakakibara et al. (1996) in a lightly loaded jet.

Fig. 10d compares the smoothing curve (representing the expected time-averaged trend – Eq. (10)) with the time-averaged volume flux measured for both unforced (Aísa et al. (2002)) and forced jets. On the other hand, *time-averages* (experimental) and the *smoothing* (adjusted from phase-averages) display the same pattern, with differences between them below 17%.

In general, the evolution of the time-averaged axial volume flux (Fig. 10d) along the jet centerline displays a fast decay near the nozzle exit ($x/D < 4$) for all cases. These results are in agreement with those reported by Longmire and Eaton (1992) and Aísa et al. (2002) even for phase-averages. This behavior is interpreted as a directional classification caused by the injection at the nozzle. Photograph 12b shows that, initially, the particles exit the nozzle with a wide jet spread angle, but this angle decreases rapidly downstream; Lázaro and Lasheras (1992a,b) have also observed these features in a free shear layer.

After a rapid decay of axial particle volume flux near the nozzle, significant differences between the unforced and the forced jets can be seen in Fig. 10d. The unforced case shows a moderate, continuous change in the slope, probably associated with some dispersion effects due to the original jet spread angle, the gas turbulence and particle collisions (García (2000)). On the contrary, in the

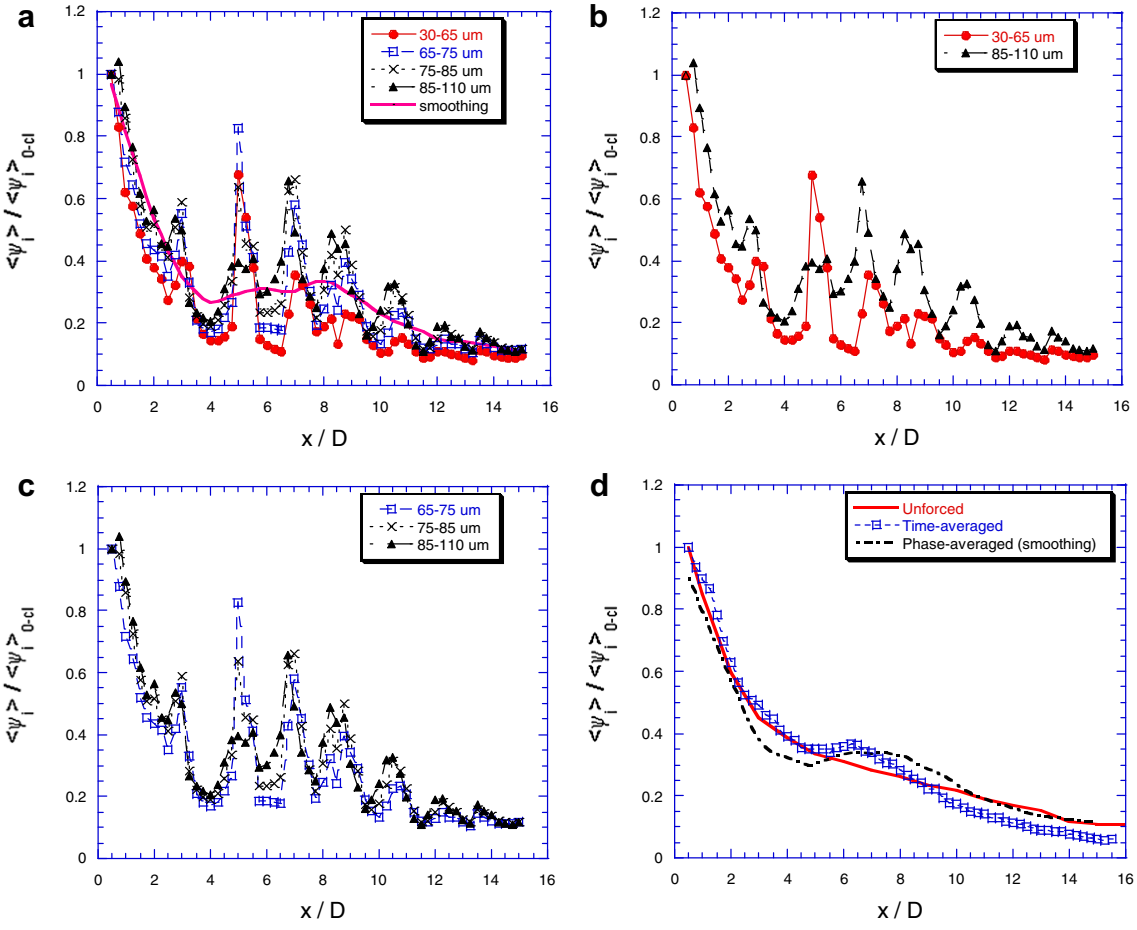

Fig. 10. Evolution of the phase-averaged axial particle volume flux along the jet centerline. (a) Different particle size classes and the average over all the particle sizes. (b) Comparison between the volume flux for the smallest and biggest particles. (c) Comparison among the bigger ones. (d) Comparison with time-averages.

region $5 < x/D < 8$, the time-averaged axial volume flux values in the forced jet are higher than those for the unforced one. This feature coincides with the high peaks observed in phase-averages (Fig. 10a), associated with the return of small particles to the jet centerline induced by vortical structures (centrifugal effects). The opposite effect is observed downstream ($x/D > 9$). Should drag force be the only mechanism responsible for the evolution of the particle volume flux, both unforced and forced cases should show rather similar trends and this increment would not have been observed. The unforced and forced jets differ in the magnitude of the coherent structures, at least in the near flow field. This leads to think that vortices can play an important role in trapping smaller particles, and convecting them along spiral trajectories; some particles do return to the mean flow field, increasing the axial volume flux, while others are expelled away, reducing its concentration downstream. Chung and Troutt (1988), Lázaro and Lasheras (1992b), and Martin and Meiburg (1994) have also observed this effect in *tongue-shaped structure*, pictorially shown in Fig. 14.

Fig. 11 represents the evolution of phase-averaged axial volume flux and axial velocities for all particle sizes, as well as gas-phase velocities. The volume flux is normalized with its own maximum value at the nozzle exit (0-cl), and velocities with the maximum gas-phase axial velocity at the nozzle exit. These results indicate that: (i) there is a clear synchronism between oscillations (both in phase and wavelength); and (ii) the oscillations (differences between peaks and valleys) in particle axial volume flux display larger amplitudes than those for particle velocity. Thus, volume flux oscillations must be likely and partially due to variations in particle velocities. This is confirmed by the visualizations in Fig. 12, depicting concentration structures (cluster-like pattern) that match the volume flux peaks.

3.3. Radial profiles within a vortical structure

Fig. 13 shows the radial semi-profiles of the time-averaged axial volume flux. Data for x = 2.5D (30 mm), 5D (60 mm), 7.5D (90 mm) and 10D (120 mm) have been taken from Aísa et al. (2002). Additionally, the time-averaged radial semi-profile at 3.75D (45 mm) for the forced jet, measured in the present work, is plotted; this axial location corresponds to the middle plane of two consecutive peaks observed in phase-averaged axial volume flux (Figs. 10 and 11). The radial coordinate (r) is normalized with the radius at which the axial volume flux is one half the value at the jet centerline ($\psi(r_{1/2}) = \frac{1}{2}\psi_{cl}$).

The radial profiles in Fig. 13 display remarkable similarities as the jet evolves. Only in the external zone of the jet, where vortical structures play an important role, the forced case ($x/D = 3.75$) shows slightly higher values.

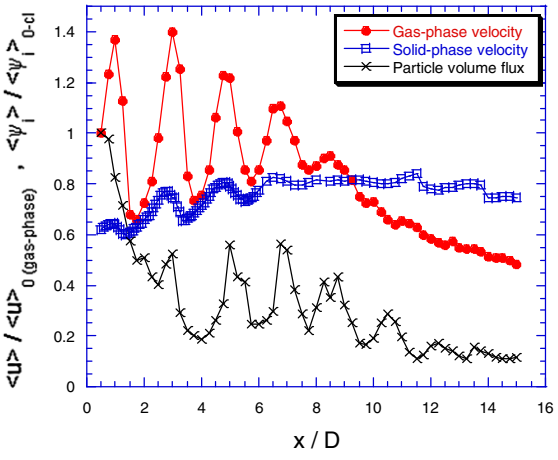

Fig. 11. Evolution of the gas and solid phase properties.

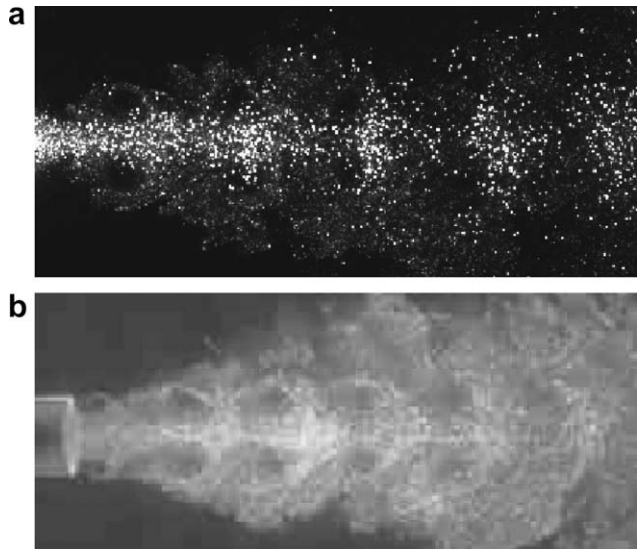

Fig. 12. Photographs of the jets. (a) Only glass beads. (b) Alumina and glass beads simultaneously.

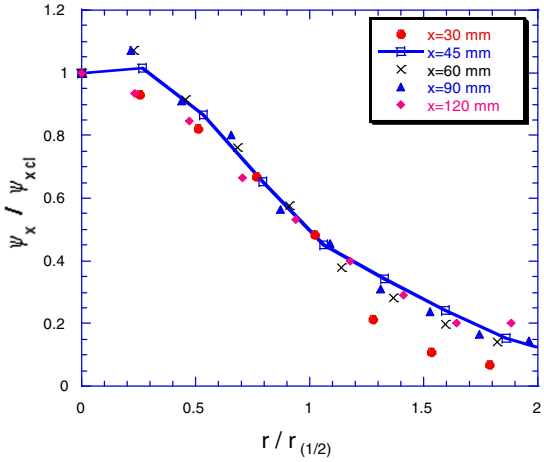

Fig. 13. Semi-profiles of the time-averaged axial volume flux at different cross sections. $r_{(1/2)}$ is the radial coordinate where the axial volume flux is a half of its value at the jet centerline. x = 30, 60, 90 and 120 mm were obtained from the unforced case (Aísa et al.). Results at x = 45 mm belong to the forced jet (present work).

To follow a vortex, phase-averages are obtained at five different cross-stream sections. As sketched in Fig. 14, variables at these sections (named S1, S2, S3, S4 and S5) are spatially correlated due to the vortical structure.

Fig. 15 depicts a zoom at the jet core of the radial semi-profiles of particle phase-averaged axial velocities. This zoom is necessary to visualize the differences among the profiles. Gas-phase axial velocities are used to normalize solid-phase axial velocities, so that the magnitude of the axial slip velocities at each radial position can be directly estimated. It is important to point out that the axial slip velocities diminish in the jet core ($r/D < 0.4$) as the jet evolves, up to section S3. After that, the axial slip velocities at the jet core increase again (from S3 to S5). This indicates that the particle Reynolds number (based on the relative slip velocity) is larger at the jet core, in sections S1 and S5. The axial drag forces are, thus, not negligible in these sections due to the large particle–gas relative velocity. On the other hand, in the vortex core ($0.5 < r/D < 0.8$),

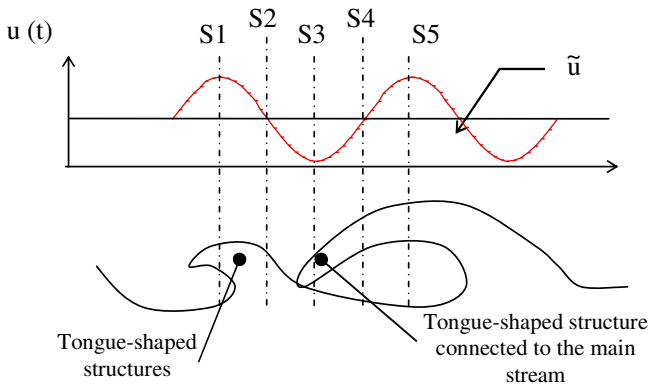

Fig. 14. Sketch of the oscillations observed in Fig. 11 and their location relative to a vortex structure. S1, S2, S3, S4 and S5 indicate the measured sections, and correspond to x/D = 3, 3.4, 3.75, 4.3 and 4.75, respectively.

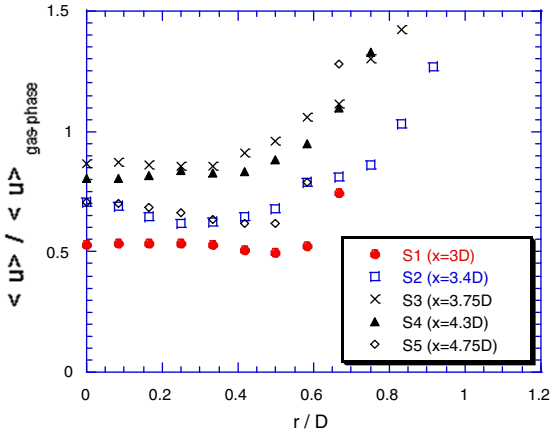

Fig. 15. Radial semi-profiles of the phase-averaged axial velocities at five different sections along the vortex structure.

the axial slip velocities are very low for all sections. These results are opposite to those found by Sakakibara et al. (1996); the difference can be ascribed to the characteristics of the vortices generated by the forcing and the loading mass ratio. In any event, axial drag forces in the present work are less important inside the vortices because of the low relative velocities.

Axial slip velocities increase again in the outer region of the jet ($r/D > 0.8$), but the particle dispersion is probably due to its own inertia and centrifugal forces (particles are propelled out the flow) because here the particle velocity is larger than the flow velocity and almost constant (Fig. 17d), as Sakakibara et al. (1996) also found at the jet exit.

It is impossible to detect any solid particle beyond $r/D > 0.7$ in section S1, whereas valid data for the solid-phase are obtained up to much longer radial distances in the downstream section (S2). This confirms that section S1 coincides with the vortex core region, characterized by a low particle concentration as shown in Photograph 12b.

The semi-profiles of the phase-averaged axial volume flux at the same five sections are shown in Fig. 16. The results plotted in Fig. 16a are normalized as in Fig. 13. The time-averaged axial volume flux at section S3 ($x/D = 3.75$) is also shown for comparison. In Fig. 16b the absolute values are presented in order to analyse behaviors that might be masked by the use of dimensionless variables. As a reference, absolute values of the phase-averaged radial velocities of the particles are also displayed in Fig. 16c.

In general, no similarities can be appreciated among the radial profiles of Fig. 16a. This is attributed to the different importance of the various forces acting on the particles, depending on the investigated section. This means that, probably, other particle dispersion effects besides inertia and drag might also be relevant. For example, the profiles shown in Fig. 16a indicate the existence of a selective process along the vortex evolution: at section S1, the highest concentrations are detected at the jet centerline, determined by the exit conditions (particle focalization). However, a peak appears at the edge of the vortex structure ($r/r_{1/2} \approx 1.3$). This is indicative of a significant influence of the large-scale structures in this region. Martin and Meiburg (1994) obtained a similar effect in the computation of a mixing layer, observing a peak in particle concentration near the vortex edge (the same region as in the present work) due to some particles being aligned with the extensional direction of the strain rate; this effect is observed even for particles with $St > 10$.

Fig. 16a also reveals that, as the vortex evolves, the peak in particle concentration shifts slightly away from the jet core (more visible in Fig. 16b) and particles near the jet centerline move faster in the radial direction (Fig. 16c). Again, particle concentration in the jet core diminishes from S1 to S3 owing to some particles being trapped and convected around by the vortex structure; axial volume flux increases from S3 to S5 as particles reincorporate into the main stream. This increment does not occur outside the jet core, where the axial volume flux continues diminishing.

As the next vortex structure is reached, particle radial velocity decreases at the jet centerline. This is in agreement with the idea that clusters are located in high strain regions (Fig. 12b), and that centrifugal effects enhance particle dispersion (Lázaro and Lasheras (1992b), and Martin and Meiburg (1994)).

At the adjacent vortex structure (S5), particles concentrate at the jet centerline as in section S1 (previous structure), but volume flux values are lower (Fig. 16b). Some particles interacting with the vortex structures are displaced away from the jet core, especially those of larger sizes. However, in general, particle concentration at S5 is higher than at S2, S3 and S4 indicating that a new particle cluster is forming.

Fig. 17a–c present the semi-profiles of the axial volume flux for different size classes at different sections. For comparison, gas-phase axial velocity profiles are also included to observe the gas/particle interaction pertaining to the flow structure. In order to discuss these results, the axial slip velocity profiles are also shown (Fig. 17d). Phase-averaged axial volume flux is normalized with the axial volume flux at the jet centerline ($\langle \gamma_{xi} \rangle_{cl}$) for every particle size. Radial position is again normalized with the nozzle diameter, D, in all Figures to relate particle behavior to vortex structures. Only sections S1, S3 and S5 are plotted, as results at S2 and S4 do not add significant information.

A decrease of the axial volume flux in section S1 near the jet core for all particle sizes can be seen in Fig. 17a. This pinpoints the influence of the initial conditions, since section S1 is quite close to the nozzle exit ($x/D = 3$) and the jet spread angle is still visible (photograph 12b). As the radial distance increases in section S1, very important differences among size classes become apparent. Concentration increases with particle size. In fact, large particles show the highest axial volume flux values. It is worth noticing that near the vortex edge ($r/D \sim 0.4$), concentration increases for all particle sizes. Martin and Meiburg (1994) observed that as the particle size becomes larger, concentration diminishes in this flow region. Should inertia or axial drag forces dominate particle motion, more gradual evolutions would be expected; thus, other forces are thought to be also relevant in this region. Finally, in the vortex core ($0.5 < r/D < 0.8$) particle concentration diminishes and the Reynolds number also decreases due to lower axial slip velocities (Fig. 17d). Therefore, although viscous effects are poten-

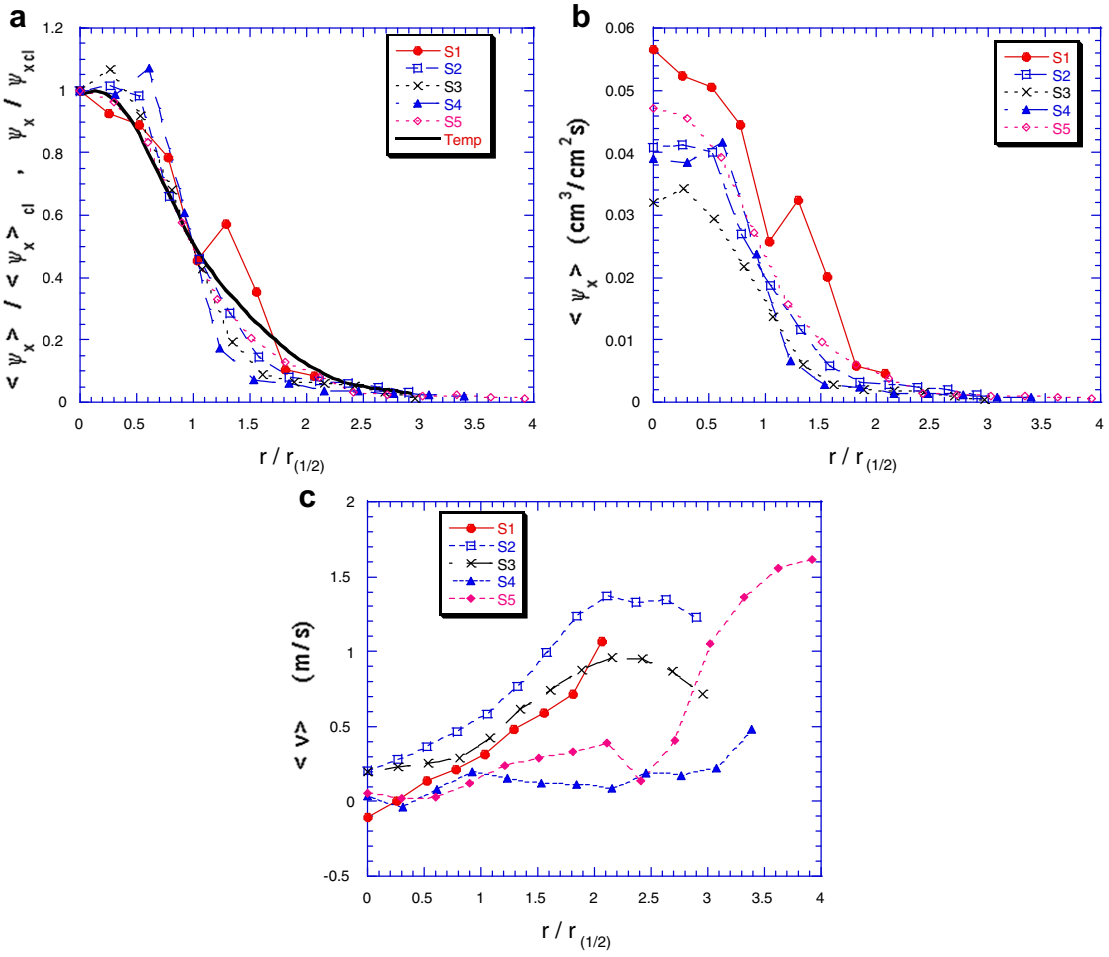

Fig. 16. Radial semi-profiles at different sections. (a) Normalized phase-averaged axial volume flux; for comparison, time-averaged values at section S3 (x = 45 mm) are also shown. (b) Absolute values of phase-averaged axial volume flux. (c) Particle phase-averaged radial velocities.

tially important (low Reynolds number and high particle drag coefficient, C_D), gas and particles have similar velocities ($\langle u_g \rangle \approx \langle u_p \rangle$), and, thus, axial drag forces can be discarded as the dominant mechanism in particle dispersion inside the vortex core.

In section S3, remarkably similar profiles are obtained for all size classes (Fig. 17b). Nevertheless, it should be noticed that the maxima of the volume fluxes are slightly off the centerline, except for the smaller size class. At this section (S3), the lowest slip velocity is also found at the jet core (Fig. 17d), indicating a closer coupling of gas and solid phases and, therefore, small axial drag forces. Since radial velocities are also low near the jet core, inertial effects are expected to be an important mechanism contributing to a significant particle concentration in these regions. On the contrary, higher radial velocities in the external zone of the main stream (Fig. 16c) suggest that particle–vortex interactions are not negligible in this region.

In section S5 (Fig. 17c), the axial volume flux profiles also depict a gradual decay with the radial distance, but the maximum values are located at the jet centerline for all size classes. The differences among axial volume flux values increase again at larger radii, especially for the largest particles. Small particles show a more pronounced decrease as the vortex core is reached, while the largest ones display a weak attenuation. This behavior is similar to that encountered in section S1.

In general, differences among size classes in particle axial volume flux are more apparent in sections with large spatial gradients of the gas axial velocity (S1 and S5) than in those displaying lower values. S1 and S5 are regions of high azymuthal vorticity and S3 is a region of high strain. Spatial gradients of the axial velocity are likely to have a strong influence on the mechanisms leading to particle dispersion.

3.4. Radial volumetric flow rate along the vortical structure

Fig. 18 represents the semi-profiles of the radial volumetric flow rate (g_r) along the vortex structure. Between sections S1 and S2, the radial volumetric flow rate (g_r) increases monotonically with the radial coordinate. The slope of the curve initially augments with the radial distance, being much higher at the edge of the vortex ($0.3 < r/D < 0.5$) than near the jet centerline; this is followed by a progressive reduction in the slope at the vortex core ($0.5 < r/D < 0.8$). As shown in Fig. 15, the slip velocity between phases diminishes inside the vortex structure ($0.5 < r/D < 0.8$); drag forces are, therefore, relatively small in those regions, and, again, are insufficient to explain the change of slope at $r/D \sim 0.5$.

Away from the vortex cores, the radial volumetric flow rate diminishes. Some negative values are obtained near the jet axis between S3 and S4, which is in agreement with inward radial velocities observed in Fig. 16c. The negative values should be interpreted as particles reincorporated to the main stream. This feature can be explained in terms of the vortex captured in photograph 12b where the tongue-shaped structures are already connected with the main stream.

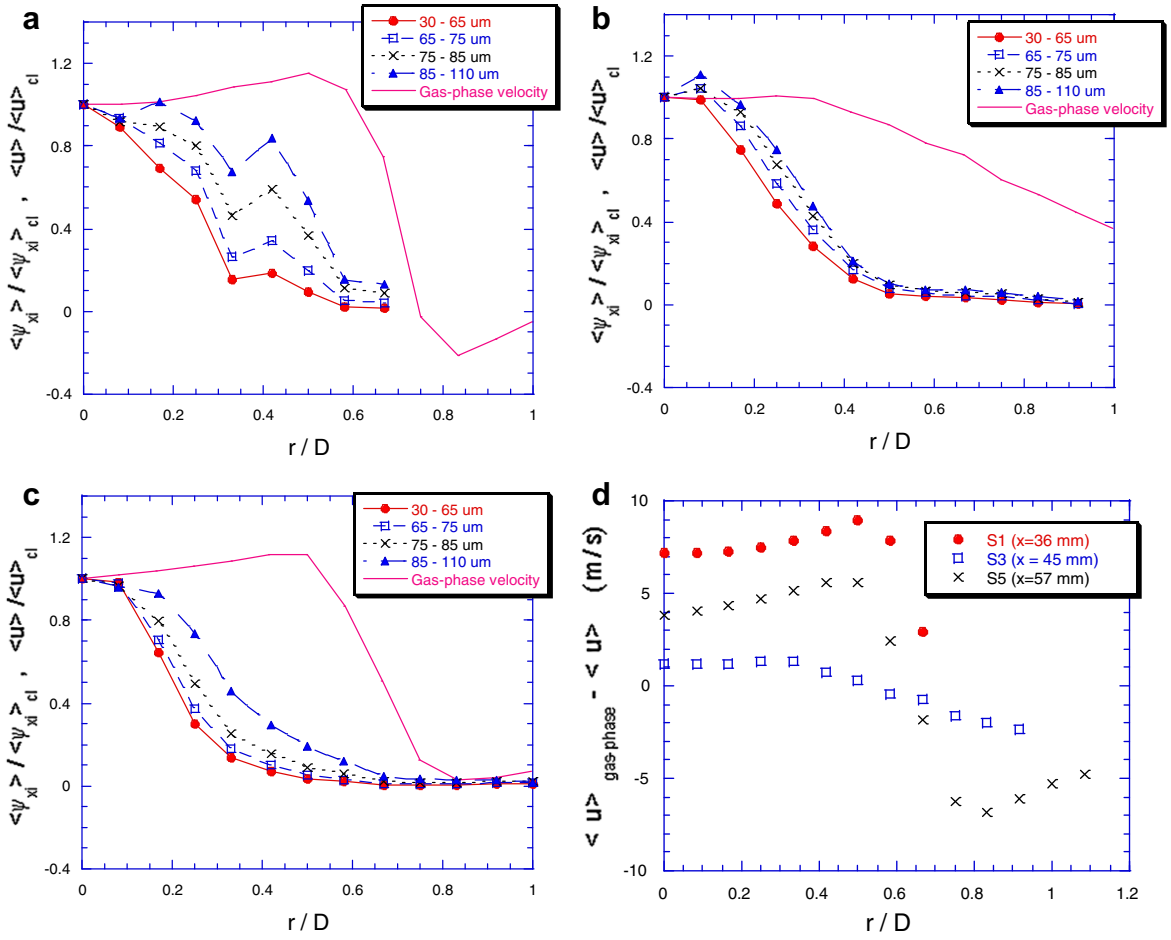

Fig. 17. Semi-profiles of the phase-averaged axial volume flux in three different sections along a vortical structure. (a) S1, (b) S3 and (c) S5. Gas-phase velocities are shown for comparison and the results with the value at the centerline. (d) Gas and solid phases velocity differences.

Between sections S4 and S5 the radial volumetric flow is negative at every radius. This is an indication that the next cluster is already reached and more particles are found in the final section (S5) rather than in the initial section (S4).

The radial dispersion can be seen in Fig. 19 in terms of the radial volumetric flow rate (g_{ri}) for different size classes. In general, these results confirm that radial volumetric flow is driven by the vortex structure; however, in this case neither centrifugal effects nor drag forces are the dominant mechanisms since the higher radial volumetric flow values are found in the vortex core, where low flow velocities are found.

Small radial volumetric particle flows and minor differences between size classes are detected near the jet centerline. However, as the vortex core is reached, the radial volumetric flow increases in region S1–S2 (Fig. 19a). In fact, the radial volumetric flow rate in the vortex core is an order of magnitude greater than at the jet centerline. These effects cannot be explained by inertial effects, because of the large particle acceleration observed in this region (Fig. 16c).

A discrete increase in the radial volumetric flow rate with the radial coordinate is also observed between the other two sections (Fig. 19b). Comparisons with Fig. 19a suggest that very few particles leave the control volume.

Especially interesting is the behavior observed in Fig. 19c. The radial volumetric flow rate of larger particles shows slightly negative values at $r/D \sim 0.2$, implying that more of those are detected in section S4 than in S3. This is in agreement with Sakakibara et al. (1996) and with Fig. 10a–c, where the larger the size the higher the spatial delay in concentration.

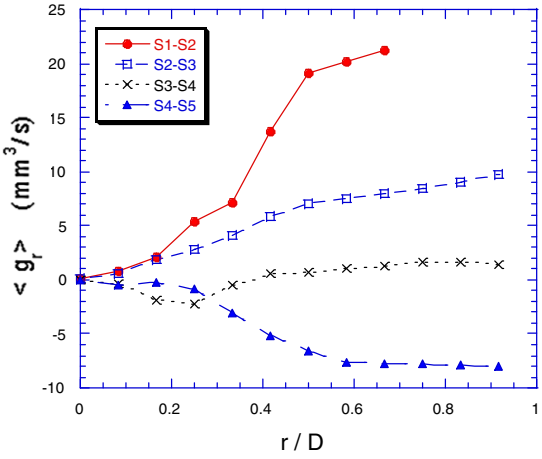

Fig. 18. Semi-profiles of the phase-averaged radial volumetric flow rate (all particle sizes) at different sections across a vortex structure.

In general, particles move away from the jet centerline, even when radial flow velocities are negligible. The particle dynamics is more intense in the vortex core and observations strongly supports the idea that the inertial and drag effects may not be as important as previously thought in these regions.

3.5. Radial forces acting along the vortical structure

The presented results tend to suggest that there may exist dispersion mechanisms, other than those classically considered, especially in the vortex core. Bagchi and Balachandar (2002a,b), Cherukat et al. (1999), Kurose and Komori (1999) and You et al. (2003) have observed that spatial gradients of the axial velocities, as those measured in the vortex core, may induce particle dispersion through Saffman and Magnus effects. This seems to coincide with the present findings in which the drag force in the vortex core regions is apparently not important. In order to gain further insight, the relative magnitudes of these effects acting on the particles located in this region are analyzed, comparing its magnitude with the radial drag force exerted by the vortical structures.

Fig. 20 depicts the Reynolds numbers (Re) calculated at sections S1 and S5, where large spatial gradients of gas-phase axial velocities (Fig. 17a and c), and high radial volumetric flow rates are detected (Fig. 18). In general, the relative Reynolds number is high and, thus, conditions for Stokes drag ($Re \ll 1$) are not fulfilled. However, very low axial slip velocities are found in the core of vortical structures, and it is, therefore, expected that particles and vortex interact for a significant period of time (compared to the characteristic flow time).

Based on the work of Maxey and Riley (1983), the particle aerodynamic and flow characteristic times take the simplified form for large ρ_p/ρ_g ratio

$$t_p = \left[\frac{3}{4}\frac{C_D}{d_p}\frac{\rho_g}{\rho_p}|\langle u_p\rangle - \langle u_g\rangle|\right]^{-1} \tag{11}$$

and

$$t_g = \frac{l_c}{U_c} = \frac{b_{1/2}}{u^o} \tag{12}$$

$b_{1/2}$ (the radial location where the velocity is one half of that at the jet centerline: $\langle u\rangle(b_{1/2}) = 0.5\cdot\langle u\rangle_{cl}$) has been selected as the characteristics length of the turbulence and u^0 (the phase-averaged axial rms fluctuation of the gas-phase) as the characteristic velocity. The drag coefficient is calculated including the Oseen correction,

$$C_D = \frac{24}{Re}\left(1 + \frac{3}{16}Re\right)^{1/2}; \quad Re = \frac{d_p|u_g - u_p|}{\nu} \tag{13}$$

which is valid for Re < 100.

The particle characteristic time is not expected to be a constant: it varies as the gas-particle relative axial velocities change.

Fig. 21 represents the Stokes number, defined as the ratio between the particle aerodynamic and flow characteristic times, $S_t = t_p/t_g$, at sections S1 and S5 and for every size class. These results can be helpful to assess the role of the different mechanisms influencing the particle motion. For example, the magnitude of the relative Reynolds number (Fig. 20) in the vortex core suggests that the sign of the radial Saffman force changes, causing the particles to travel from high to low velocity zones (Kurose and Komori (1999), Bagchi and Balachandar (2002a)). This is contrary to the expected behavior sketched in Fig. 1.

On the other hand, the high Stokes number observed in Fig. 21 indicates a slow particle response to flow fluctuations. Moreover, the high spatial gradients of the axial velocity detected in the gas-phase lead to speculate that lift forces due to Saffman and

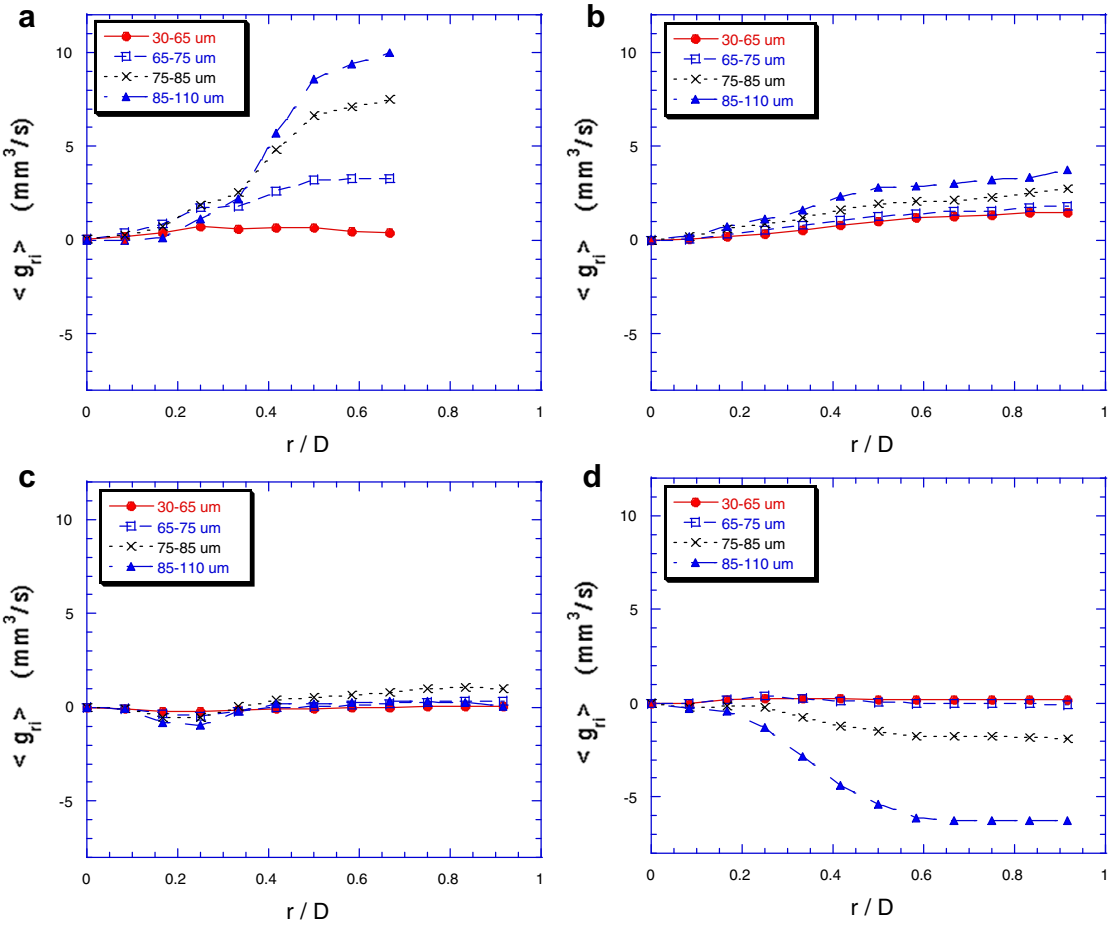

Fig. 19. Semi-profiles of radial volumetric flow along the vortex structure. Different size classes. (a) From S1 to S2. (b) From S2 to S3. (c) From S3 to S4. (d) From S4 to S5.

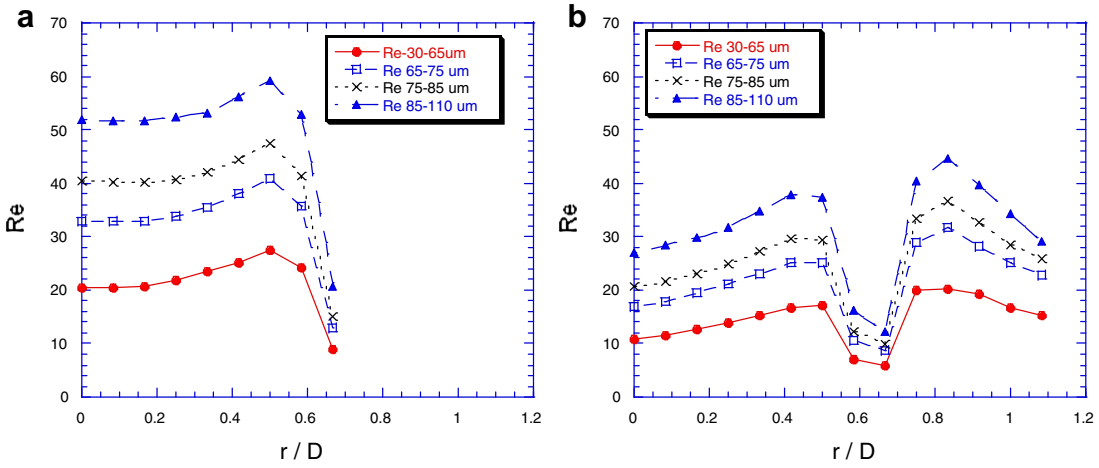

Fig. 20. Relative Reynolds numbers at sections with high spatial gradients of the axial velocity. (a) Section S1. (b) Section S5.

Magnus effects might play an important role in the dispersion of the particles. Along this line of reasoning, Bagchi and Balachandar (2002a) have analogously reported an important increase in the lift coefficient, C_L, for relative Reynolds number in the intermediate range (5–100).

Since vortex shedding is acoustically forced at 400 Hz, the characteristic time between two vortical structures is estimated to be of the order of 2.5 ms. According to Bagchi and Balachandar (2002a), the rotational motion reaches equilibrium faster than the translational one, and the characteristic time of 2.5 ms might be enough for the particle to attain a steady rotation induced by the surrounding fluid. However, due to the impossibility to determine the particle rotation rate, Ω_p, the two limit cases can be considered: particle rotating with the ambient fluid ($\Omega_p = 0.5G$; G stands for the dimensional shear rate of the surrounding flow) and negligible particle rotation ($\Omega_p = 0$).

In order to obtain an order of magnitude of both Saffman and Magnus effects, it is first considered that the spatial velocity gradient in both sections S1 and S5 is linear for $0.5 < r/D < 0.8$ (Fig. 17a and c). In this region, the gradient is approximately $G_{S1} = 5878.87$ (s^{-1}) and $G_{S5} = 3827.3$ (s^{-1}) for S1 and S5, respectively.

The range of the main dimensionless parameters required to evaluate Saffman and Magnus effects are presented in Tables 2 and 3 for S1 and S5, respectively. The following definitions are used

$$Re = \frac{d_p u_{rel}}{\nu}; \quad Re_G = \frac{G \cdot d_p^2}{\nu}; \quad Re_\Omega = \frac{\Omega_p d_p^2}{\nu} = \frac{1}{2} Re_G; \quad \varepsilon = \frac{\sqrt{Re_G}}{Re}; \quad s = \frac{Re_G}{Re}$$

where $u_{rel} = (\langle u_f \rangle - \langle u_p \rangle)$ is the axial slip velocity and ν is the kinematic viscosity.

It is apparent from Tables 2 and 3 that neither the maximum value for ε nor the shear based Reynolds number, Re_G, are small compared to unity. This implies some corrections to the lift coefficient, C_L, employed to calculate the Saffman force

$$F_{Saff} = \frac{1}{8} \pi C_L \rho d_p^2 u_r^2 \tag{14}$$

Taking into account the second-order Saffman force for moderate values of ε,

$$C_L = \frac{12.92}{\pi} \varepsilon - \frac{11}{8} \varepsilon \sqrt{Re_G} \tag{15}$$

McLuaghlin (1991) has extended Saffman's analysis, and Mei (1992) has suggested for $0.1 < \varepsilon < 20$ the following expression

$$\frac{C_L}{C_{L(Saff)}} = 0.3(1 + \mathrm{Tanh}[2.5 \mathrm{Log}_{10}(\varepsilon + 0.191)])(0.667 + \mathrm{Tanh}[6(\varepsilon - 0.32)]) \tag{16}$$

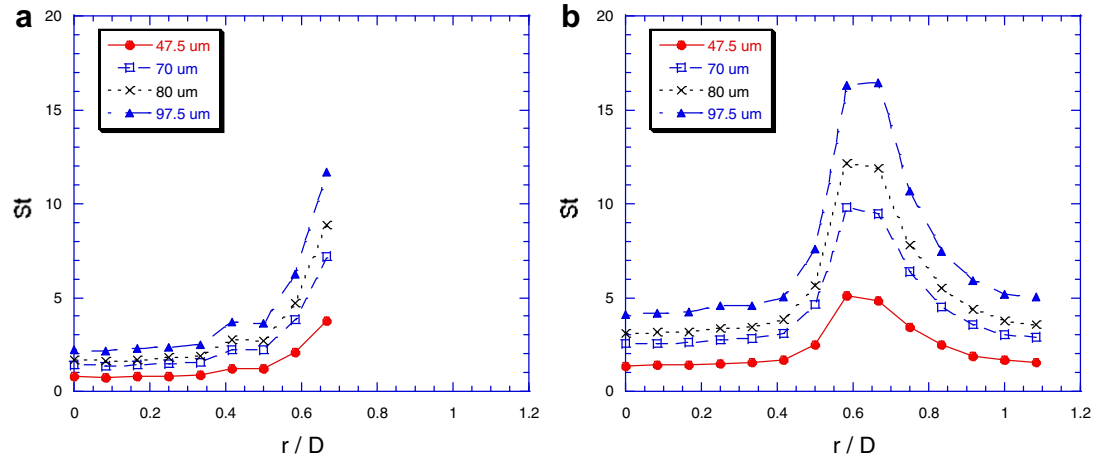

Fig. 21. Stokes number at sections with high spatial gradients of the axial velocity. (a) Section S1. (b) Section S5.

Moreover, Mei (1992) has also proposed the finite Reynolds number approximations

$$\frac{C_L}{C_{Saff}} = \begin{cases} (1 - 0.3314(\frac{s}{2})^{1/2})e^{-Re_p/10} + 0.3314(\frac{s}{2})^{1/2}; & \text{for } Re_p \leqslant 40 \\ 0.0524\left(\frac{s \cdot Re_p}{2}\right)^{1/2}; & \text{for } Re_p > 40 \end{cases} \tag{17}$$

On the other hand, the rotation induced lift force known as Magnus effect is estimated by You et al. (2003). They have obtained an approximate relationship for the lift coefficient, valid for $Re_p < 68.4$, in terms of the dimensionless rotational speed of a spherical particle, $\Omega^* = \frac{\Omega_p d_p}{2u_r} < 5$. The lift coefficient then takes the form

$$C_L = A(1 - B^{\Omega^*}) \tag{18}$$

where

$$A = 1.51 + 5.69\exp(-Re_p/18.62) + 26.32\exp(-Re_p/3.65)$$
$$\text{and} \quad B = 0.56 + 0.37\exp\left(-\frac{Re_p - 0.5}{26.39}\right) \tag{19}$$

It is worth remarking that the numerical result of the Magnus force obtained through Eq. (18) is very similar to that calculated taking into account the lift coefficient determined by Bagchi and Balachandar (2002a).

Both Saffman and Magnus forces are shown for sections S1 and S5 in Tables 4 and 5, respectively. As a reference, the drag force (F_{Dr}) in the radial direction,

$$F_{Dr} = \frac{1}{8}\pi\rho C_D d_p^2(\langle v\rangle_f - \langle v\rangle_p)^2 \tag{20}$$

is also calculated. The radial drag coefficient is estimated using Eq. (13). The signs in Tables 4 and 5 denote the r-direction. Notice that the radial drag force varies by an order of magnitude from point $r/D = 0.5$ to $r/D = 0.58$. This can be explained by the high radial slip velocities in sections S1 and S5 (see Fig. 22).

In addition, the results in Tables 4 and 5 indicate that the Saffman force is at least 4 times the value of the Magnus force. Hence, in the present case the shear-induced force seems to be more important than the rotation-induced one. This is consistent with the results obtained by Bagchi and Balachandar (2002), Kurose and Komori (1999) who observed that particle rotation (Magnus effect) has a negligible influence on the total lift force. Furthermore, the calculations indicate that the Saffman force is comparable or greater than the radial drag. In some instances, the Saffman force can attain values up to 10% of those of the axial drag. The lift force has, therefore, an important influence on the radial particle dispersion, especially for large particles. This is consistent with the experimental results observed along the jet centerline. Moreover, while Magnus force is directed toward the main stream, Saffman force is directed in a positive r-direction instead.

As shown in Fig. 15, a low axial slip velocity is measured at the vortex core (S1 and S5, $0.5 < r/D < 0.8$). As a consequence, particles detected within the vortex core at S1 are expected to remain for distances of the order of one or several vortex diameters. The estimated value of Saffman forces is considered a reasonable estimation of the magnitude of the lift force over a significant period of time (compared to the characteristic flow time). According to the analysis performed, the order of magnitude of the Saffman lift is comparable to that of the force required to cause the measured change of radial velocity between sections S1 and S5.

Another important result from Tables 4 and 5 is that the Saffman force is always directed towards the outer part of the jet, away from the main stream. This is at odds with the numerical results of Bagchi and Balachandar (2002b); they have computed the vortex-induced lift force in a flow, which mimics the main features of the present work. They have observed the Saffman lift and the Magnus force directed always to the higher velocity stream. These differences might be due to the fact that these authors have assumed that the vortex rotates as a solid body but particles were held fixed and not allowed to translate, while Longmire and Eaton (1992) and Cerecedo et al. (2004) have demonstrated that this assumption is not completely correct. The fact that particles do not translate could also make important differences. In fact, Bagchi and Balachandar (2002b) have recognized that their simulations did not exactly reproduce the experimental observations because the idealised solid body rotation is only a crude approximation and they suggest that their findings should only be qualitatively compared. The results in Tables 4 and 5 are, on the other hand, consistent with the behavior observed at the vortex core in the present work. Radial forces can induce the large particle radial acceleration observed in Fig. 16c.

Table 2
Parameters related to the Saffman and Magnus effects at Section S1

Particle size class (μm)	Re_p (max–min)	Re_G	ε (max–min)
30–65	27.5–8.9	0.884	0.105–0.034
65–75	40.8–12.8	1.920	0.108–0.034
75–85	47.5–15.1	2.508	0.104–0.033
85–110	59.3–20.8	3.726	0.092–0.033

The maximum value of ($s = Re_G/Re$) is observed at the vortex core.

Table 3
Parameters related to the Saffman and Magnus effects at Section S5

Particle size class (μm)	Re_p (max–min)	Re_G	ε (max – min)
30–65	20.1–6.0	0.576	0.127–0.037
65–75	31.7–8.7	1.250	0.129–0.035
75–85	36.7–9.8	1.633	0.130–0.035
85–110	44.6–12.1	2.425	0.128–0.035

The maximum value of ($s = Re_G/Re$) is observed at the vortex core.

Table 4
Estimation of the lateral lift force (F_L) at section S1

Particle size class (μm)	Position	F_{Saff}	F_{Mag}	F_{Dr} (radial)	F_{LSaff}/F_{Dr}	F_{LMag}/F_{Dr}
30–65	$r/D = 0.5$	3.6E-09	−9.0 E-10	1.0 E-08	0.33	−0.08
	$r/D = 0.58$	3.0 E-09	−7.0 E-10	7.7 E-08	0.04	−0.01
65–75	$r/D = 0.5$	1.0 E-08	−2.5 E-09	1.7 E-08	0.67	−0.14
	$r/D = 0.58$	1.0 E-08	−2.0 E-09	1.3 E-07	0.08	−0.01
75–85	$r/D = 0.5$	1.7 E-08	−3.5 E-09	2.0 E-08	0.86	−0.17
	$r/D = 0.58$	1.5 E-08	−2.6 E-09	1.5 E-07	0.10	−0.02
85–110	$r/D = 0.5$	3.2 E-08	−6.0 E-09	2.8 E-08	1.15	−0.21
	$r/D = 0.58$	2.9 E-08	−4.8 E-09	1.9 E-07	0.15	−0.02

Comparison with the radial drag force (F_{Dr} (radial)). Force values are in Newtons (N). The sign in lift force indicates the r-direction.

Table 5
Estimation of the lateral lift force (F_L) at section S5

Particle size class (μm)	Position	F_{Saff}	F_{Mag}	F_{Dr} (radial)	F_{LSaff}/F_{Dr}	F_{LMag}/F_{Dr}
30–65	$r/D = 0.5$	1.5 E-09	−4.7 E-10	7.3 E-10	2.04	−0.64
	$r/D = 0.58$	6.1 E-10	−1.1 E-10	1.4 E-08	0.04	−0.01
65–75	$r/D = 0.5$	4.6 E-09	−1.3 E-09	1.8 E-09	2.60	−0.73
	$r/D = 0.58$	1.9 E-09	−2.8 E-10	2.2 E-08	0.09	−0.01
75–85	$r/D = 0.5$	7.0 E-09	−1.8 E-09	1.4 E-09	5.01	−1.32
	$r/D = 0.58$	3.0 E-09	−3.8 E-10	2.5 E-08	0.12	−0.01
85–110	$r/D = 0.5$	1.3 E-08	−3.2 E-09	9.3 E-10	14.25	−3.45
	$r/D = 0.58$	5.7 E-09	−7.0 E-10	3.1 E-08	0.19	−0.02

Comparison with the radial drag force (F_{Dr} (radial)). Force values are in Newtons (N). The sign indicates the r-direction.

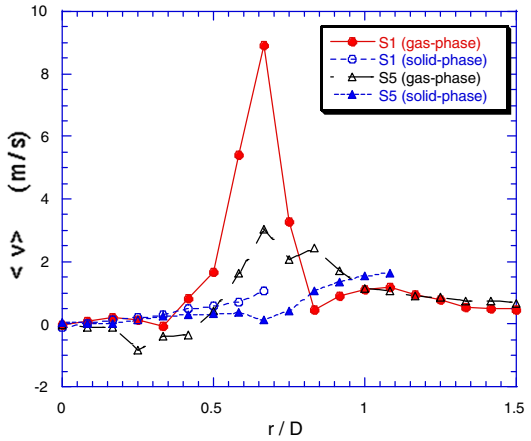

Fig. 22. Phase-averaged radial velocities of both single- and solid-phases at sections S1 and S5.

The reduction of large size particles in the axial volume flux supports the idea that they undergo pronounced radial displacements.

This analysis emphasizes the fact that shear flows can induce non-negligible lateral forces as other researchers have proposed. These forces can play a significant role as a particle dispersion mechanism. As a consequence, the understanding and modeling of particle dynamics in two-phase jets must include, besides an accurate description of the large-scale structures, a correct treatment of Saffman and Magnus effects. Otherwise, particle dispersion and/or accumulation phenomena might not be adequately reproduced, should the gas-particle interactions be only ascribed to drag forces.

4. Conclusions

The influence of large-scale structures on particle dispersion in the near field of a two-phase jet has been investigated. The flow has been acoustically forced at 400 Hz in order to control large vortices. Two types of statistics (time- and phase-averages) have been used to derive relevant information on flow-particle interactions. Time-averages have been selected to compare the unforced (Aísa et al. (2002)) and the forced jets (present work). Phase-averages have enabled *freezing* the jet structures and analyzing the local particle concentration at five sections along the spatial evolution of two consecutive vortices. This has been effective to unmask some particle dispersion mechanisms hidden by time-averages.

Although jet conditions at the nozzle exit are affected by particle focalization, the axial volume fluxes at the jet exit for all size classes display similar profiles when normalized with their own values at the jet centerline. This similarity has also been observed in phase-averaged statistics. This can be interpreted as a homogeneous contribution of all particle sizes to the bulk particle mass flux injected at the nozzle exit, consistent with the results of Hayashi and Branch (1980).

The evolution of time-averaged axial velocities of the gas and particles along the jet centerline suggests an important interaction between both phases, involving different mechanisms. Very near the exit nozzle ($x/D < 4$) and at the jet core, drag forces and a directional classification due to the jet spread angle drive particle concentrations. These mechanisms lead to an increase of the time-averaged mean particle velocity and a fast decay of particle concentration, as Aísa et al. (2002) pointed out for the same but unforced jet. This feature has also been observed in the present work for the *instantaneous* behavior along the jet centerline, using phase-averaged results. However, once tongue-shaped structures are connected to the main stream (as sketched in Fig. 14), an increase in the axial volume flux by small particles that are convected from the outer zone to the inner part of the jet has been observed, with a decrease in the contribution of large size particles.

Time-averaged axial volume fluxes show similarities at different sections across the jet for both the forced and unforced cases. However, these similarities disappear when the instantaneous structure of the jet is analyzed through the phase-averages. Relevant conclusions can be drawn from the near flow field profiles of axial volume fluxes and radial volumetric flow rates along a vortical structure; in the region occupied by a vortex, the influence of large spatial gradients of the axial velocity seems to be the most important feature affecting the large particle dispersion.

Since the most important differences in axial volume fluxes have been found in sections with large spatial gradients of the gas-phase axial velocity, coinciding with the vortex cores where low slip velocities are found, particle dynamics in these regions is thought to be controlled by other mechanisms than drag. Saffman and Magnus effects have been scrutinized in these sections displaying high radial gradients of axial velocities and, in order to gain further insight, the magnitudes of them have been estimated. In particular, the Saffman lift is found to be comparable, or greater than radial drag forces in the vortex core. Moreover, in some cases the value of the Saffman force can be up to 10% of that of the axial drag. This implies that the lift force bears an important influence on the radial particle dispersion, especially for large particles. This is consistent with results observed along the jet centerline. On the other hand, centrifugal effects disperse the smaller particles, confirming previous observations by several authors.

The present results indicate that particle/flow interaction in the jet outer region is largely driven by large-scale structures, and that particle dispersion and/or accumulation phenomena cannot be adequately explained if only drag forces are considered.

Acknowledgements

The authors are grateful to the referees for their invaluable comments and criticism and to Prof. César Dopazo for carefully reading and correcting various versions of the manuscript. They are also indebted to Dr. Ignacio García for his help with the access to instrumentation.

References

Aísa, L., García, J.A., Cerecedo, L.M., García-Palacín, I., Calvo, E., 2002. Particle concentration and local mass flux measurements in two-phase flows with PDA. Application to a study on the dispersion of spherical particles in turbulent air jet. Int. J. Multiphase Flow 20, 301–324.

Anderson, S.L., Longmire, E.K., 1995. Particle motion in the stagnation zone of an impinging air jet. Int. J. Fluid Mech. 229, 333–366.

Bagchi, P., Balachandar, S., 2002a. Effect of free rotation in the motion of a solid sphere in linear shear flow at moderate Reynolds. Phys. Fluids 14, 2719–2737.

Bagchi, P., Balachandar, S., 2002b. Shear versus vortex-induced lift force on a rigid sphere at moderate Re. J. Fluid Mech. 473, 379–388.

Cerecedo, L.M., Aísa, L., García, J.A., Santolaya, J.L., 2004. Changes in a coflowing jet structure caused by acoustic forcing. J. Exp. Fluids 36, 867–878.

Cherukat, J.B., McLaughlin, J.B., Dandy, D.S., 1999. A computational study of the inertial lift on a sphere in a linear shear flow field. Int. J. Multiphase Flow 25, 15–33.

Chung, J.N., Troutt, T.R., 1988. Simulation of particle dispersion in an axisymmetric jet. J. Fluid Mech. 186, 199–222.

García, J.A., (2000). Experimental study on an axisymmetric laden two-phase jet. Particle Concentration and Dispersion (in Spanish), Ph.D. Dissertation, University of Zaragoza.

Hayashi, K., Branch, M.C., 1980. Concentration, velocity and particle size measurements in gas-solid two-phase jet. AIAA J. Energy 4, 193–198. Sept.–Oct..

Kurose, R., Komori, S., 1999. Drag and lift forces on a rotating sphere in a linear shear flow. J. Fluid Mech. 384, 183–206.

Lázaro, B.J., Lasheras, J.C., 1992a. Particle dispersion in the developing free shear layer. Part 1. Unforced flow. J. Fluid Mech. 235, 143–178.

Lázaro, B.J., Lasheras, J.C., 1992b. Particle dispersion in the developing free shear layer. Part 2. Forced flow. J. Fluid Mech. 235, 179–221.

Longmire, E.K., Eaton, J.K., 1992. Structure of a particle-laden round jet. J. Fluid Mech. 236, 217–257.

Martin, J.E., Meiburg, E., 1994. The accumulation and dispersion of heavy particles in forced two-dimensional mixing layer. I. The fundamental and subharmonic cases. Phys. Fluids 6, 1116–1132.

Maxey, M.R., Riley, J.J., 1983. Equation of motion for a small rigid sphere in a nonuniform flow. Phys. Fluids 26, 883–889.
McLuaghlin, J.B., 1991. Inertial migration of a small sphere in linear shear flows. J. Fluid Mech. 234, 261–274.
Mei, R., 1992. An approximate expression for the shear lift force on a spherical particle at finite Reynolds number. Int. J. Multiphase Flow 18, 145–147.
Park, C.J., Chen, L.D., 1989. Experimental investigation of confined turbulent jets. Part I: Single-phase data. AIAA J. 27, 11.
Prévost, F., 1994. Comportement des Particules Solides Polydispersees dans un Jet D'Air Turbulent. Tesis doctoral, INP Universidad de Toulouse, Francia.
Roisman, I.V., Tropea, C., 2000. Drops distributions and flux measurements in sprays using the phase doppler technique. In: 10th International Symposium on Applications of Laser Techniques to Fluid Mechanics, Lisbon, pp. 1–12.
Sakakibara, J., Wicker, R.B., Eaton, J.K., 1996. Measurements of the particle-fluid velocity correlation and the extra dissipation in a round jet. Int. J. Multiphase Flow 22, 863–881.
Sbrizzai, F., Verzicco, R., Pidria, M.F., Soldati, A., 2004. Mechanisms for selective radial dispersion of microparticles in the transition region of a confined turbulent round jet. Int. J. Multiphase Flow 30, 1389–1417.
Swanson, T.R., Richards, C.D., 1997. The structure of an acoustically forced, droplet-laden jet. Atomization Spray 7, 561–579.
Widmann, J.F., Presser, C., Leigh, S.D., 2001. Improving phase Doppler volume flux measurements in low data rate applications. Measurement Sci. Technol. 12, 1180–1190.
You, C., Qi, H., Xu, X., 2003. Lift force on rotating sphere at low reynolds numbers and high rotational speed. ACTA Mechanica SINICA, Chinese Soc. Theoret. Appl. Mech. 19, 300–307.